Applied Catalysis B: Environmental 192 (2016) 101–107

Contents lists available at ScienceDirect

Applied Catalysis B: Environmental

journal homepage: www.elsevier.com/locate/apcatb

New understanding on the different photocatalytic activity of wurtzite and zinc-blende CdS

Jinfeng Zhang[a,b], S. Wageh[c], AhmedA. Al-Ghamdi[c], Jiaguo Yu[a,c,*]

[a] State Key Laboratory of Advanced Technology for Materials Synthesis and Processing, Wuhan University of Technology, Wuhan 430070, PR China
[b] Department of Physics and Electronic Information, Huaibei Normal University, Anhui, Huaibei 235000, PR China
[c] Department of Physics, Faculty of Science, King Abdulaziz University, Jeddah 21589, Saudi Arabia

ARTICLE INFO

Article history:
Received 20 January 2016
Received in revised form 18 March 2016
Accepted 24 March 2016
Available online 25 March 2016

Keywords:
Wurtzite CdS
Photocatalytic activity
Effective masse
Internal electric field

ABSTRACT

In general, wurtzite CdS exhibits a higher photocatalytic activity than zinc-blende CdS. However, the underlying physicochemical reasons responsible for the differences of photocatalytic activity between the wurtzite and zinc-blende CdS are still unclear. In this work, the structural characteristics, band structures, density of states, bond populations, optical properties and charge carrier effective mass of wurtzite and zinc-blende CdS were investigated based on first-principle theoretical calculations. The calculated results indicate that the distortion of CdS_4 tetrahedron units results in the formation of internal electric field in wurtzite CdS, which is beneficial for the efficient separation and diffusion of photogenerated charge carriers. Contrarily, the internal electric field is absent in zinc-blende CdS. Moreover, the effective masses of photogenerated charge carriers of wurtzite CdS are smaller than those of zinc-blende CdS, implying faster migration of photogenerated charge carriers to perform photocatalytic reactions on wurtzite CdS surfaces. All the above factors result in the lower recombination rate of photogenerated charge carriers within wurtzite CdS. Therefore, it is not surprising that wurtzite CdS usually shows a higher photocatalytic activity than zinc-blende CdS. This investigation will provide some new understanding on the difference of photocatalytic activity between wurtzite and zinc-blende CdS.

1. Introduction

With extensive industrialization development and rapid population growth, the energy crisis and environment pollution caused by the depletion of fossil fuels are regarded as two major challenges in the future [1–8]. To address these issues, solar energy harvesting is a promising strategy to realize sustainable energy production for human society [9–11]. Fabricating Functional Devices that can convert the energy of sunlight into chemical bonds plays a crucial role in achieving this objective since it represents a real opportunity to produce chemical fuels at low environmental and economic costs [12–15]. During the past decades, many semiconductor photocatalysts have been reported to be effective in hydrogen generation from water under light irradiation [16–21]. Especially, CdS has been extensively studied because of its narrow band gap (2.4 eV) that matches well with the visible light spectrum of sun and suitable band edge positions for reducing H_2O to H_2 [22–26]. Generally, CdS has two common crystalline phases, namely the wurtzite and zinc-blende phase [27]. Compared with zinc-blende CdS, the wurtzite CdS has been studied more intensively because it is more stable and can be synthesized easily by various preparation methods [28]. For example, Matsumura et al. reported that wurtzite CdS displayed a higher activity for photocatalytic hydrogen production than zinc-blende CdS [27]. In addition, Bao et al. successfully tuned the crystal structure of wurtzite and zinc-blende CdS via a simple cadmium–thiourea complex thermolysis route, which further demonstrated the superiority of wurtzite CdS in photocatalysis [29]. However, to the best of our knowledge, the underlying physicochemical mechanism responsible for the difference of photocatalytic activity between wurtzite and zinc-blende CdS still remains ambiguous. Much more direct evidences concerning the photocatalytic activity difference between the wurtzite and zinc-blende CdS are expected to be obtained through further theoretical calculations.

Although the light absorption capacity of wurtzite and zinc-blende CdS are nearly same due to their similar band gaps (2.36 eV for zinc-blende CdS and 2.32 eV for wurtzite CdS), the photocatalytic hydrogen productionactivity of wurtzite CdS is obviously

* Corresponding author at: State Key Laboratory of Advanced Technology for Materials Synthesis and Processing, Wuhan University of Technology, Wuhan 430070, PR China.
E-mail addresses: jiaguoyu@yahoo.com, yujiaguo93@163.com (J. Yu).

http://dx.doi.org/10.1016/j.apcatb.2016.03.058
0926-3373/

superior to that of zinc-blende CdS [29–31]. The previous explanation ascribed the higher photocatalytic activity of wurtzite CdS to its smaller crystalline size, larger specific surface area and higher surface adsorption capacity than those of zinc-blende CdS [29]. As well known, the implementation of semiconductor photocatalytic reactions consists of three main steps: (1) light absorption, (2) exciton dissociation and (3) charge carrier diffusion [32,33]. These steps largely depend on the intrinsic properties of the semiconductor photocatalysts such as their band gaps, exciton binding energy and charge carrier effective masses [33–35]. Therefore, it is necessary to investigate the electronic structures and calculate the charge carrier effective masses of photocatalysts to better understand the difference of photocatalytic performance between the wurtzite and zinc-blende CdS. However, to our knowledge, little research has been performed on the effect of effective mass of photogenerated electrons and holes on the photocatalytic hydrogen production activity of wurtzite and zinc-blende CdS.

In theory, first-principle density functional theory (DFT) calculation has been proved to be generally accurate in the theoretical prediction of structure parameters and ground states structure type, aiming to become an efficient way to investigate the various physical and chemical properties of photocatalytic materials as an effective complement to experiment [36]. However, precise calculation of electronic structure by DFT methods is currently a major challenge [37]. For example, the generalized gradient approximation (GGA) and local density approximation (LDA) functionals most extensively applied usually underestimate the semiconductor band gaps by about 30–100% compared with experimental results [38]. This underestimation of band gap is closely related to the inherent lack of derivative discontinuity and delocalization error in the exchange–correlation functional derivative [39–41]. Several other methods have been adopted to overcome the limitations of GGA and LDA with respect to electronic structure properties. For instance, the B3LYP and PBE0 hybrid functionals incorporate 20% and 25% Hartree–Fock exchange functional, respectively, which demonstrate more accuracy and present a significant improvement over the previous GGA and LDA functionals [42,43]. Due to the overestimation of band gap values by Hartree-Fock exchange functional, the hybrid B3LYP and PBE0 density functionals can generally give more accurate band gap values and provide more precise descriptions of electronic structures of semiconductors.

In this work, we, for the first time, used both the standard functions (LDA and PBE) and hybrid functions (B3LYP and PBE0) to perform DFT calculation of the structural characteristics, energy band structures, density of states (DOS), projected density of states (PDOS), chemical bonding and optical properties of wurtzite and zinc-blende CdS. The effective masses of photogenerated electrons and holes were further calculated based on the obtained energy band structures. Notably, the internal electric field in wurtzite CdS crystal structure was found due to the deformation of CdS_4 tetrahedron. The effects of charge carrier effective mass, electronic dipole moment, and internal electric field on the photocatalytic activity of wurtzite and zinc-blende CdS were investigated and discussed. This investigation will provide some new insights into the photocatalytic activity difference between wurtzite and zinc-blende CdS photocatalysts.

2. Computational details

Three periodic dimensional calculations in this work were carried out using the plane-wave pseudopotential method based on standard DFT and hybrid–DFT, as applied in the Cambridge Serial Total Energy Package (CASTEP) code [44]. The norm-conserving pseudopotential was used for describing the interaction between the valence electrons and the ionic core. The kinetic energy cutoff for the plane-wave expansion was set to 650 eV for standard and hybrid DFT calculations. The Monkhorst-Pack scheme k-point grids for standard DFT functionals were respectively set as $7 \times 7 \times 4$ and $4 \times 4 \times 4$ for wurtzite and zinc-blende CdS, the corresponding parameter settings for hybrid DFT functionals were $4 \times 4 \times 2$ and $2 \times 2 \times 2$ for wurtzite and zinc-blende CdS, respectively. The geometry structures of different phase CdS were optimized by the Perdew-Burke-Ernzerhof (PBE) of GGA and LDA exchange correlation function. The convergence criteria for the energy change, maximum force, maximum stress, and maximum displacement tolerances were respectively set to 1.0×10^{-5} eV per atom, 0.03 eV per Å, 0.05 GPa, and 1.0×10^{-3} Å, through the Broyden, Fletcher, Goldfarb, Shanno (BFGS)-based method [45]. The valence electrons were taken into account for CdS corresponding to Cd: $4s^2 4p^6 4d^{10} 5s^2$ and S: $3s^2 3p^4$, while the remained electrons were kept frozen as core states. In order to confirm the accuracy of the calculations, the higher cutoff energy and bigger k-points were adopted, the results of energy and geometry structure shows almost no change. After finishing the geometry optimizations, the electronic structures of wurtzite and zinc-blende CdS were respectively calculated by LDA, GGA, B3LYP and PBE0 hybrid functionals.

Table 1
The optimized lattice parameters and their relative deviations of wurtzite and zinc-blende CdS.

Species	Parameter	a = b (Å)	c (Å)	α = β (°)	γ (°)
Wurtzite CdS	Exp[a]	4.121	6.682	90	120
	PBE	4.258	6.909	90	120
	Deviation (%)	3.2	3.3	0	0
	LDA	4.138	6.716	90	120
	Deviation (%)	0.4	0.5	0	0
Zinc-blende CdS	Exp[b]	5.832	5.832	90	90
	PBE	6.009	6.009	90	90
	Deviation (%)	3.0	3.0	0	0
	LDA	5.840	5.840	90	90
	Deviation (%)	0.1	0.1	0	0

[a] Ref. [46].
[b] Ref. [47].

3. Results and discussion

3.1. Electronic properties

The conventional unit cells of the wurtzite and zinc-blende CdS are shown in Fig. 1. The crystal structures of wurtzite and zinc-blende CdS belong to the space group of $P6_3mc$ and F-43m, respectively. In this investigation, the experimental values of lattice parameters are regarded as the starting data, and both the atomic coordinates and the lattice constants are optimized. The optimized structural parameters and their relative deviations of wurtzite and zinc-blendeCdS calculated by the GGA and LDA methods are listed in Table 1. It is clear that the results of the GGA method are overestimated as compared to the experimental results, whereas the values determined by the LDA method are more consistent with experimental values. The deviations between the results calculated by LDA method and experimental values are within 0.5%, indicating the higher reliability of geometry optimization by the LDA function. Therefore, in the following discussion, we will focus on the calculated results based on the structural optimization by the LDA function.

In order to understand the structure–property relationships of wurtzite and zinc-blende CdS photocatalyst materials, it is necessary to investigate their crystallographic structure in details. The atomic coordinates of wurtzite CdS are Cd at the site of (1/3, 2/3, 0) and S at (1/3, 2/3, 3/8), belonging to a close-packed hexagonal wurtzite (CPH) structure. The zinc-blende CdS has a face-centered

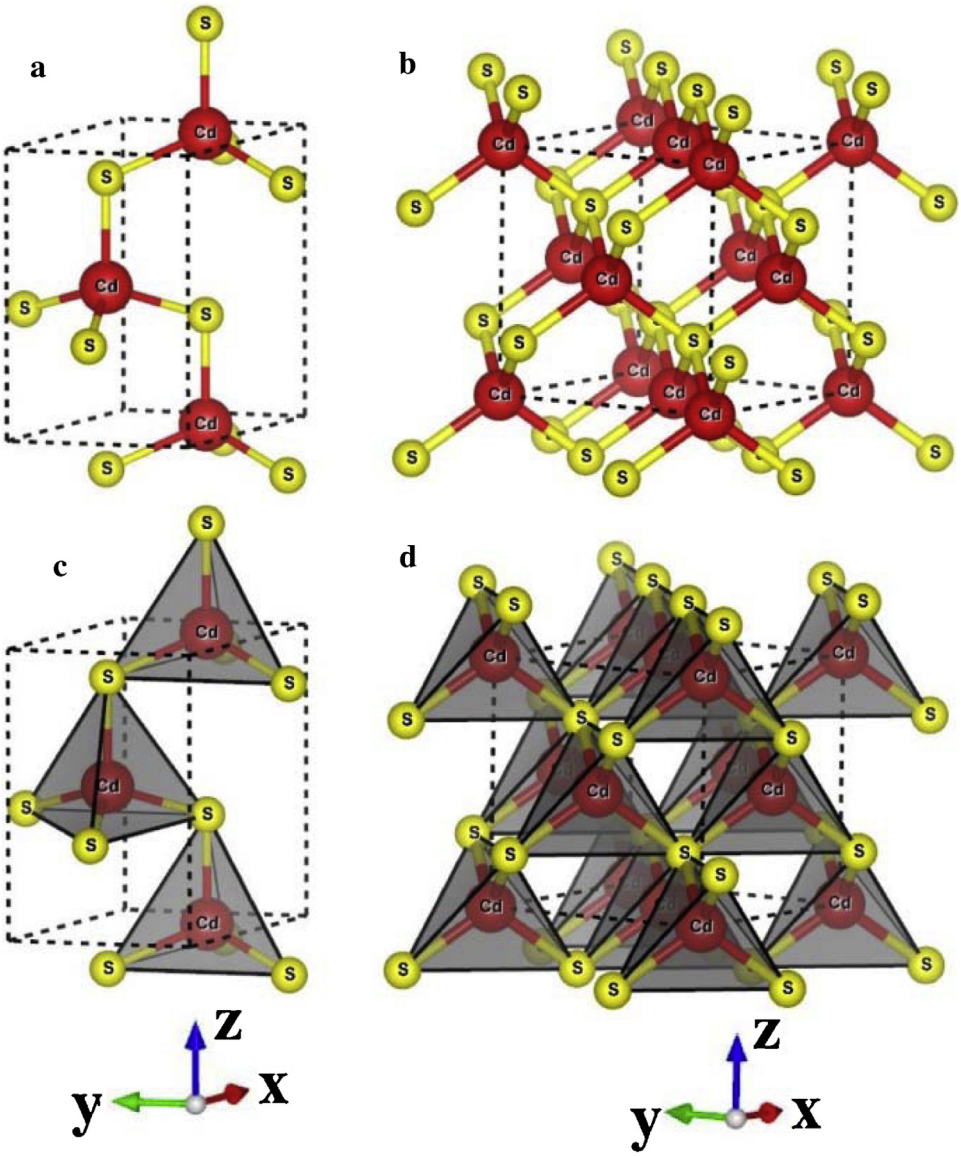

Fig. 1. Schematic diagram of the wurtzite and zinc-blende CdS crystal structures. a and b are the ball and stick models of wurtzite and zinc-blende CdS, respectively; c and d are the polyhedron models of wurtzite and zinc-blende CdS, respectively.

cubic (FCC) structure with Cd occupying the position at (0, 0, 0) and S at (1/4, 1/4, 1/4). These two different phases possess the same CdS_4 tetrahedron as their basic structural units. Each Cd atom is coordinated with four surrounding S atoms in a tetrahedral fashion, while four adjacent CdS_4 tetrahedron units are linked together by one S atom correspondingly. However, despite these similarities, their stacking patterns of Cd-S bilayers are different, A-aB-bA-aB-b for the wurtzite CdS and A-aB-bC-cA-aB-bC-c for the zinc-blende CdS, where capital letters denote pure Cd planes and small letters pure S planes or *vice verse* [14,48].

To further analyze the origin of different photocatalytic activities between wurtzite and zinc-blende CdS, the energy band structures were calculated by using PBE of GGA, LDA, B3LYP and PBE0 functionals as shown in Fig. 2(a-h). The Fermi level is set at zero shown as a dashed line. It is clear that both wurtzite and zinc-blende CdS belong to direct band gap semiconductors with their conduction band minimum (CBM) and valence band maximum (VBM) located at the same G point. In general, the nature of the band gap (i.e., direct or indirect) plays a significant role in determining the absorption coefficient of the semiconductor [49].

Table 2
The band gaps of wurtzite and zinc-blende CdS calculated by standard DFT and hybrid DFT.

Species	Exchange-correlation function	LDA	PBE	B3LYP	PBE0
Wurtzite	E_g(eV)	1.34	1.45	2.5	2.83
	Deviation (%)	−40.0	−39.0	5.9	19.9
Zinc-blende	E_g(eV)	1.26	1.38	2.54	2.88
	Deviation (%)	−46.0	−41.0	9.0	24.0

The direct band gap semiconductors are more advantageous in terms of optical absorptivity compared with those indirect ones, since the indirect transition of electrons requires the participation of additional phonons [50]. The calculated band gap values based on standard DFT and hybrid–DFT are both listed in Table 2. By comparing these calculated results, it is found that the band gaps calculated by the B3LYP function are closest to experimental values (2.32 eV for wurtzite CdS and 2.36 eV for zinc-blende CdS). Contrarily, the band gaps calculated by the PBE and LDA functions are much smaller than the experimental results. This is owing to the well-known underestimation effect of the PBE and LDA functions

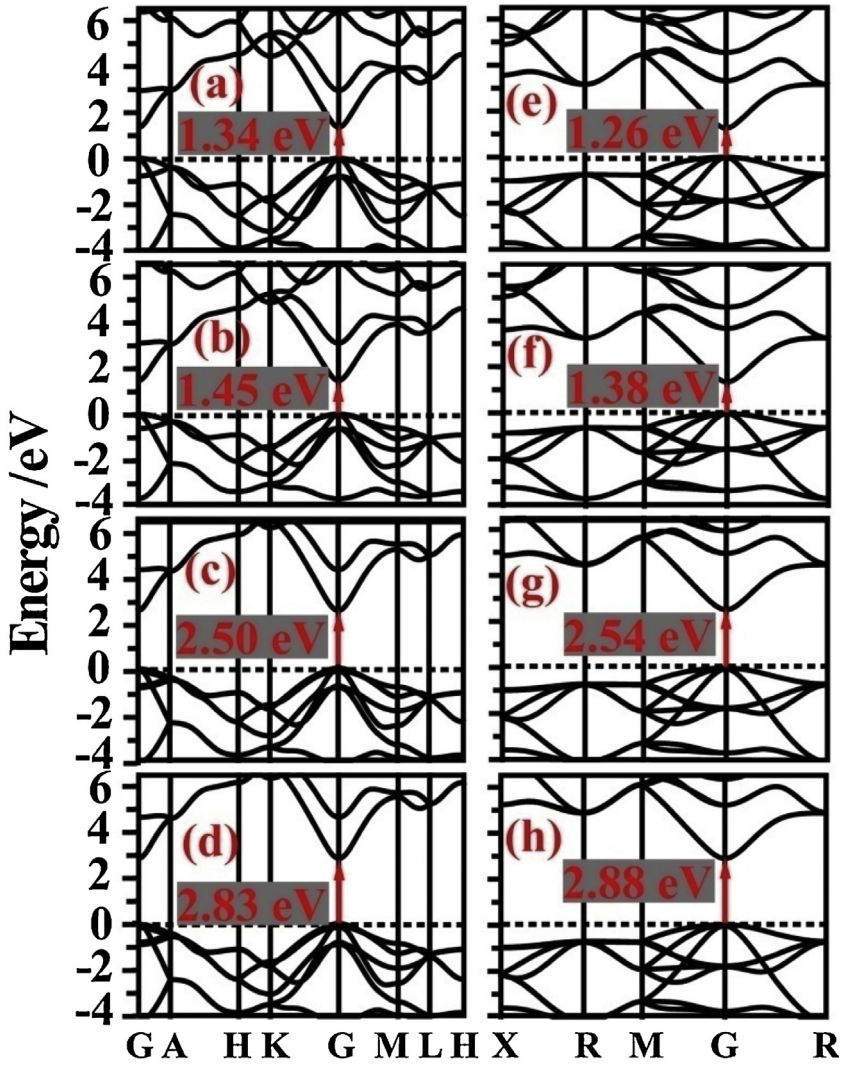

Fig. 2. The energy band structure of wurtzite (left) and zinc-blende (right) CdS calculated by LDA (a, e), PBE (b, f), B3LYP (c, g) and PBE0 (d, h) functions.

in DFT calculations [51]. Therefore, the hybrid B3LYP function can be more suitable for calculating electronic structures of wurtzite and zinc-blende CdS than LDA, GGA/PBE and PEB0 functions.

To further clarify the properties of their electronic structures, the DOS of wurtzite and zinc-blende CdS and PDOS of Cd and S elements were calculated and shown in Fig. 3. Due to the similarity in crystal structure, the calculated DOS constitutions of wurtzite and zinc-blende CdS are similar. The top of valence bands and the bottom of conduction bands primarily consist of S 3p and Cd5s states, respectively. For both wurtzite and zinc-blend CdS, the valence bands and conduction bands are composed by S 3p, Cd 5s and Cd 4p states. This implies the existence of inter-atomic sp hybridizations among Cd5s, Cd 4p and S 3p states, which form bonding and antibonding states in the valence and conduction band regions, respectively. Further observation indicates there are a few Cd 4d states in wurtzite CdS, This implies that a few Cd 4d states participating in the strong p–d hybridizations in the valance bands of zinc-blende CdS, thus resulting in the valance band widening and the VBM moving upward slightly. As a result, the band gap of wurtzite CdS (2.32 eV) is slightly smaller than that of zinc-blende CdS (2.36 eV).

To investigate the chemical bond properties of wurtzite and zinc-blende CdS, their Mulliken charges, bond lengths and bond populations were also calculated and shown in Table 3. Bond population is an important parameter to analyze ionic and covalent characters of chemical bonds. Zero bond population indicates an ideal ionic bond, while a bigger bond population value implies a higher degree of covalent interaction. As observed from the Mulliken charges, S atoms take a significant amount of electrons that are equivalently donated from Cd atoms to form Cd-S bonds. Interestingly, for the CdS_4 tetrahedron units of wurtzite CdS, the calculated Cd-S bond lengths (2.605 Å) along its [0001] direction are slightly longer than the values in other directions (2.601 Å), leading to the deformation distortion of CdS_4 tetrahedron in wurtzite CdS crystal structures. Such distortion further causes the separation of the positive (Cd) and negative (S) charge centers within CdS_4 tetrahedron units. Thus, the electronic dipole moments are created along [0001] direction of wurtzite CdS crystals structures and calculated

Table 3
The Mulliken charges, Cd—S bond populations, and lengths in the CdS_4 tetrahedron of wurtzite and zinc-blende CdS calculated by B3LYP hybrid functionals.

Species	Mulliken charge		Direction	Bond population	Bond length (Å)
	S	Cd			
Wurtzite	−0.74	0.74	[0001]	0.16	2.605
				1.32	2.601
Zinc-blende	−0.72	0.72		0.38	2.602

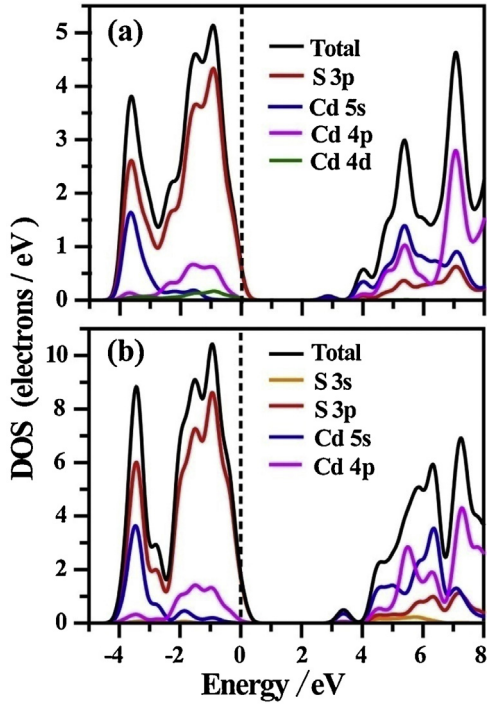

Fig. 3. The DOS calculated by B3LYP hybrid functionals for (a) wurtzite CdS and (b) zinc-blende CdS.

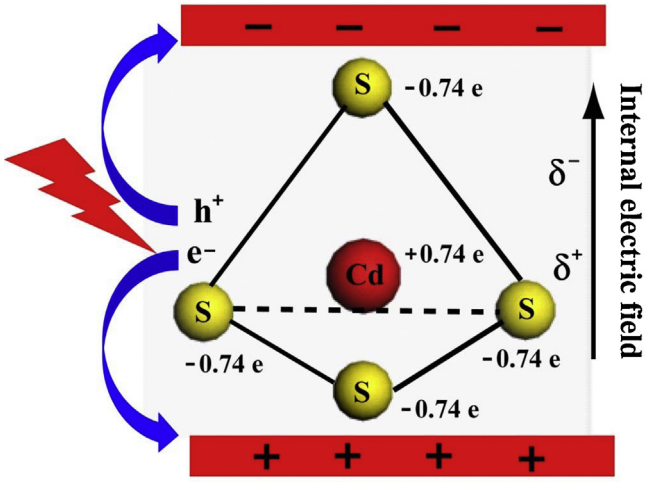

Fig. 4. Schematic diagram of internal electric field formation along [0001] direction within wurtzite CdS.

to be 0.04 D based on the atomic coordinates and the obtained Mulliken charges of S and Cd atoms. However, the Cd—S bonds (2.602 Å) in CdS_4 tetrahedron of zinc-blende CdS are homogenous in all directions, indicating the overlapping of positive (Cd) and negative (S) charge centers and the absence of electronic dipole moments. Also, the calculated bond populations (0.38) of zinc-blende CdS are equivalent. However, in wurtzite CdS, the bond populations (0.16) of the Cd—S bonds along [0001] direction are far smaller than those (1.32) in Cd-S bilayer plane, resulting in higher ionic characters along [0001] direction. The higher ionic character and electronic dipole moment along [0001] direction also result in the formation of internal electric field within wurtzite CdS, which can promote the migration and separation of photogenerated electrons and holes, as shown in Fig. 4. However, such internal electric field does not exist in zinc-blende CdS due to their homogenous Cd—S bond

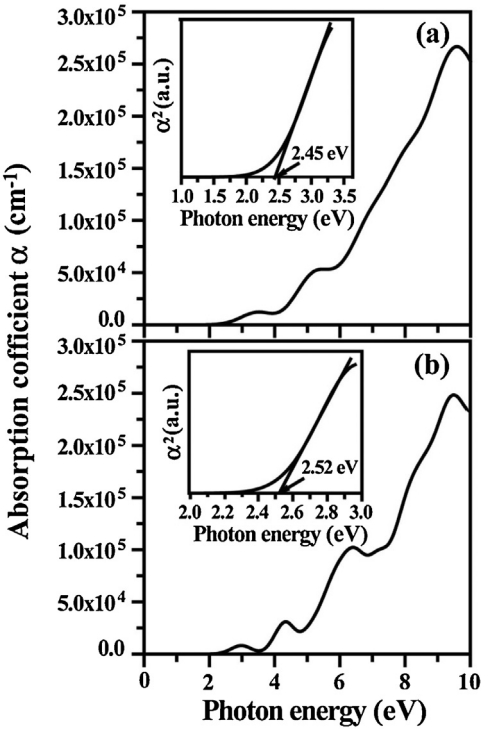

Fig. 5. The calculated absorption coefficients by the hybrid B3LYP functionals for (a) wurtzite and (b) zinc-blende CdS. Inset showing plots of the $\alpha^2(h\nu)$ against photon energy $h\nu$.

lengths [50]. It is well known that the presence of such internal electric field within crystal structures is beneficial for the efficient separation and diffusion of photogenerated charge carriers, which is very advantageous for enhancing photocatalytic activity [52]. Therefore, the photogenerated electron-hole pairs can separate more easily in wurtzite CdS. This is one of the important reasons why the wurtzite CdS usually has better photocatalytic performance than the zinc-blende CdS.

In order to investigate their optical properties, the optical absorption coefficients of both wurtzite and zinc-blende CdS were calculated, as shown in Fig. 5. In general, the optical band gaps of CdS can be estimated by the Kubelka–Munk (KM) method [53]:

$$\alpha(h\nu) = C(h\nu\text{-}E_g)^{n/2} \quad (1)$$

Here α is the optical absorption coefficient, E_g is the band gap of the semiconductor, $h\nu$ is the photon energy, and C is a constant relevant to the semiconductor property. The values of index n are determined by the semiconductor properties (n = 4 for indirect band gap semiconductors and n = 1 for direct band gap semiconductors). Since the wurtzite and zinc-blende CdS both belong to direct band gap semiconductors, the n values for wurtzite and zinc-blende CdS are 1, and thus Eq. (1) can be transformed into the following formula [54]:

$$\alpha^2(h\nu) = C^2(h\nu\text{-}E_g) \quad (2)$$

According to Eq. (2), the optical band gap of wurtzite and zinc-blende CdS can be acquired by extrapolating the linear portion of $\alpha^2(h\nu)$ against $h\nu$ plot to the point α = 0. The calculated optical band gaps (shown in the inset of Fig. 5) are 2.45 and 2.52 eV for wurtzite and zinc-blende CdS, respectively, which are approximate to the experimental values [29]. Further comparison indicates that the optical band gap of wurtzite CdS is slightly smaller than that of zinc-blende CdS, which is also consistent with the results of band structures of wurtzite and zinc-blende CdS calculated by hybrid B3LYP method.

Table 4
The effective mass of photogenerated carriers of wurtzite and zinc-blende CdS calculated by hybrid B3LYE functionals.

Species		m_e^*/m_0			m_h^*/m_0		
Zinc-blende	Direction	G → R	G → M		G → R	G → M	
	Calculation	0.079	0.068		0.940	1.150	
Wurtzite	Direction	G → K	G → M	G → A	G → K	G → M	G → A
	Calculation	0.038	0.033	0.011	0.174	0.148	0.010

3.2. Effective mass

As is well known, after the generation of photogenerated electron–hole pairs by light excitation, the diffusion and separation rates of photogenerated charge carriers play important roles in determining the quantum efficiency of photocatalytic reactions [55]. The photogenerated electrons and holes need to diffuse to the active sites on photocatalyst surfaces, where they can perform the photocatalytic reactions prior to their recombination. Thus, a greater discrepancy between the diffusion rates of photogenerated electrons and holes indicates the less recombination within these electron–hole pairs. The diffusion coefficient, D, characterizes the diffusion facility of charge carriers in a photocatalyst. Moreover, D is related to the mobility, μ, of the charge carrier according to the Einstein relation (Eq. (3)), which in turn is connected with the effective collision time (τ) and the effective mass (m^*) of charge carrier (Eq. (4)). Therefore, the mobility and diffusion coefficient of photogenerated electrons and holes can be indirectly assessed by their effective masses. In general, the mobility of photogenerated charge carriers is inversely proportional to their effective mass, indicating that smaller effective masses correspond to higher mobility of charge carriers [33].

$$D = \frac{k_B T}{e}\mu \tag{3}$$

$$\mu = e\frac{\tau}{m^*} \tag{4}$$

In order to further analyze the difference of photocatalytic activity between wurtzite and zinc-blende CdS, the effective masses of photogenerated charge carriers were calculated by fitting parabolic functions around the CBM (for the electron effective mass m_e^*) and the VBM (for the hole effective mass m_h^*) according to the following equations [56]:

$$m^* = \pm\frac{\hbar^2}{d^2E/dk^2} \tag{5}$$

where m^* is the effective mass of charge carriers, k is the wave vector, $\hbar$ is the reduced Planck constant, E is the band edge energy as a function of k, and The ± denotes that + for the electrons and − for the holes. On the basis of Eq. (5), the photogenerated charge carriers in the flat bands with nearly constant gradient possess large effective mass, while those in the disperse bands with variable gradient possess small effective mass. The region selected for parabolic fitting is within ±1 meV around the CBM or VBM to ensure accurate parabolic approximation. This method is also used to calculate the effective masses of photogenerated carriers of silver halide-based Ag@AgX(X = Cl, Br, I) [57]. The calculated results of effective masses for wurtzite and zinc-blende CdS by B3LYP approach are summarized in Table 4.

It is obvious that the calculated effective masses of photogenerated electrons of both wurtzite and zinc-blende CdS are much smaller than those of photogenerated holes in all directions. A larger effective mass difference between photogenerated electrons and holes suggests a larger difference in the charge carrier mobility [58]. Namely, the electron–hole pairs with markedly different effective mass are unsynchronized in mobility, which is beneficial for reducing the recombination of photogenerated carriers. The effective masses of electron and hole along different directions are almost equal within zinc-blende CdS because of its high symmetry. Contrarily, the effective mass of electron and hole within wurtzite CdS is only similar along the directions G → M and G → K. Moreover, the charge carrier effective mass of wurtzite CdS along G → A direction is smaller than those of other directions. This indicates the photogenerated carriers of wurtzite CdS along G → A ([0001]) direction can more easily separate and diffuse to photocatalyst surface for triggering photocatalytic reaction. This is consistent with the above discussion on the effect of internal electric field along [0001] direction within wurtzite CdS on photocatalytic activity. Further comparison reveals that the effective mass of photogenerated charge carriers within wurtzite CdS is smaller than that of zinc-blende CdS, implying the higher mobility of charge carriers of wurtzite CdS than that of zinc-blende CdS. This indicates that the photogenerated electrons and holes of wurtzite CdS more easily diffuse and transfer to the surface from its interior to participate in photocatalytic reactions due to its smaller effective mass. Therefore, it is easy to understand why wurtzite CdS shows better photocatalytic activity than zinc-blende CdS.

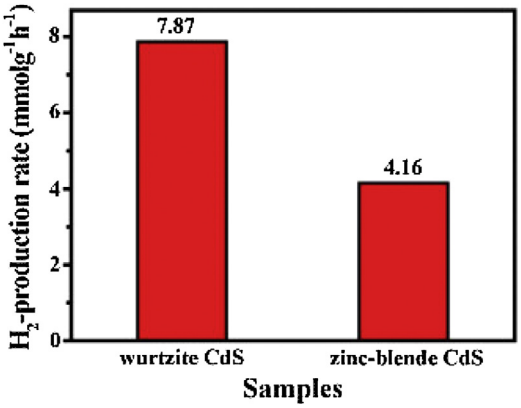

Fig. 6. Comparison of photocatalytic H_2-production activity of wurtzite and zinc-blende CdS photocatalysts prepared by hydrothermal method.

To further understand the above underlying physical mechanism of the difference of photocatalytic hydrogen production activity between wurtzite and zinc-blende CdS, We synthesized wurtzite and zinc-blende CdS photocatalysts by hydrothermal method [59], and the experimental results indicate that wurtzite CdS has a better photocatalytic H_2-production activity than zinc–blende CdS (as shown in Fig. 6). The related experimental details can be found from Supplementary data.

4. Conclusions

The structural characteristics, electronic structures, and chemical bonding of wurtzite and zinc-blende CdS were successfully calculated by the LDA and PBE of GGA, hybrid B3LYP and PBE0 functionals. The comparison of the calculated results indicate that the hybrid B3LYP function is more accurate for the calculation of electronic structures of wurtzite and zinc-blende CdS compared with LDA, PBE and PEB0 functionals. The distortion of CdS_4 tetrahedron in wurtzite CdS crystal structures leads to the formation of electronic dipole moment and internal electric field, which are beneficial to the separation and diffusion of photogenerated charge carriers. However, none of the CdS_4 tetrahedron distortion, electronic dipole moment and internal electric field is found in zinc-blende CdS. Based on the analysis of Mulliken charges and bond populations, the wurtzite CdS has stronger ionic character along [0001] direction, implying the higher charge carrier mobility and

weaker covalent characteristics along [0001] direction. Moreover, the calculated carrier effective masses of wurtzite CdS are smaller than those of blende CdS. The smaller effective mass of photogenerated electrons and holes can facilitate their mobility, reduce their recombination rate and improve photocatalytic activity in wurtzite CdS. Due to the smaller effective mass and the presence of internal electric field, not surprising, wurtzite CdS generally exhibits a higher photocatalytic activity than zinc-blende CdS. This work will provide some new insights into understanding the difference of photocatalytic activity of wurtzite and zinc-blende structure semiconductors.

Acknowledgements

This work was partially supported by the 973 program (2013CB632402), NSFC (51272199, 51320105001 and 21433007), Deanship of Scientific Research (DSR) of King Abdulaziz University (90-130-35-HiCi), Fundamental Research Funds for the Central Universities (WUT: 2015-III-034), Self-determined and Innovative Research Funds of SKLWUT (2015-ZD-1) and the Natural Science Foundation of Hubei Province of China (No. 2015CFA001) for Jiaguo Yu. This research was financially supported by NSFC (51502106), Natural Science Foundation of Education Committee of Anhui Province (KJ2014B06) and Collaborative Innovation Center of Advanced Functional Materials (XTZX103732015013) for Jinfeng Zhang.

Appendix A. Supplementary data

Supplementary data associated with this article can be found, in the online version, at http://dx.doi.org/10.1016/j.apcatb.2016.03.058.

Notes and references

[1] Q.J. Xiang, B. Cheng, J.G. Yu, Angew. Chem. Int. Ed. 54 (2015) 2–19.
[2] J.F. Zhang, Y.F. Hu, X.L. Jiang, S.F. Chen, S.G. Meng, X.L. Fu, J. Hazard. Mater. 280 (2014) 713–722.
[3] N.S. Lewis, D.G. Nocera, Proc. Natl. Acad. Sci. U. S. A. 103 (2006) 15729–15735.
[4] W.J. Ong, L.L. Tan, S.P. Cha, S.T. Yong, A.R. Mohamed, ChemSusChem 7 (2014) 690–719.
[5] J.G. Yu, J. Jin, B. Cheng, M. Jaroniec, J. Mater. Chem. A 2 (2014) 3407–3416.
[6] L. Yuan, Y.J. Xu, Appl. Surf. Sci. 342 (2015) 154–167.
[7] C.L. Lu, L. Zhang, Y.W. Zhang, S. Liu, G. Liu, Appl. Surf. Sci. 319 (2014) 278–284.
[8] H.G. Yu, F.Y. Chen, F. Chen, X.F. Wang, Appl. Surf. Sci. 358 (2015) 385–392.
[9] Q. Li, X. Li, S. Wageh, A.A. Al-Ghamdi, J. Yu, Adv. Energy Mater. 5 (2015) 1500010.
[10] R.D. Cortright, R.R. Davda, J.A. Dumesic, Nature 418 (2002) 964–967.
[11] J. Jin, J.G. Yu, D.P. Guo, C. Cui, W. Ho, Small 11 (2015) 5262–5271.
[12] X. Li, J.G. Yu, J.X. Low, Y.P. Fang, J. Xiao, X.B. Chen, J. Mater. Chem. A 3 (2015) 2485–2534.
[13] Z.G. Zou, J.H. Ye, K. Sayama, H. Arakawa, Nature 414 (2001) 625–627.
[14] K. Zhang, L.J. Guo, Catal. Sci. Technol. 3 (2013) 1672–1690.
[15] P. Zhou, J. Yu, M. Jaroniec, Adv. Mater. 26 (2014) 4920–4935.
[16] A. Kudo, Y. Miseki, Chem. Soc. Rev. 38 (2009) 253–278.
[17] L.J. Shen, M.B. Luo, Y.H. Liu, R.W. Liang, F.F. Jing, L. Wu, Appl. Catal. B: Environ. 166–167 (2015) 445–453.
[18] S. Chen, X.P. Chen, Q.Z. Jiang, J. Yuan, C.F. Lin, W.F. Shangguan, Appl. Surf. Sci. 316 (2014) 590–594.
[19] X.X. Zhou, H.R. Chen, Y.Y. Sun, K. Zhang, X.Q. Fan, Y. Zhu, Y. Chen, G.J. Tao, J.L. Shi, Appl. Catal. B: Environ. 152–153 (2014) 271–279.
[20] Q.J. Xiang, B. Cheng, J.G. Yu, App. Catal. B: Environ. 138–139 (2013) 299–303.
[21] I. Majeed, M.A. Nadeem, M. Al-Oufi, M.A. Nadeem, G.I.N. Waterhouse, A. Badshah, J.B. Metsonc, H. Idriss, Appl. Catal. B: Environ. 182 (2016) 266–276.
[22] X. Zong, H. Yan, G. Wu, G. Ma, F. Wen, L. Wang, C. Li, J. Am. Chem. Soc. 130 (2008) 7176–7177.
[23] J.G. Yu, Y.F. Yu, P. Zhou, W. Xiao, B. Cheng, Appl. Catal. B: Environ. 156 (2014) 184–191.
[24] J.F. Reber, M. Rusek, J. Phys. Chem 90 (1986) 824–834.
[25] J. Jin, J.G. Yu, G. Liu, P.K. Wong, J. Mater. Chem. A 1 (2013) 10927–10934.
[26] D. Zhao, Q. Wu, C.F. Yang, R.T. Koodali, Appl. Surf. Sci. 356 (2015) 308–316.
[27] M. Matsumura, S. Furukawa, Y. Saho, H. TsubOmura, J. Phys. Chem. 89 (1985) 1329–1330.
[28] R. Banerjee, R. Jayakrishnan, P. Ayyub, J. Phys. Condens. Matter 12 (2000) 10647–10654.
[29] N. Bao, L. Shen, T. Takata, K. Domen, A. Gupta, K. Yanagisawa, C.A. Grimes, J. Phys. Chem. C 111 (2007) 17527–17534.
[30] Y.X. Li, L.F. Tang, S.Q. Peng, Z.C. Lia, G.X. Lu, CrystEngComm 14 (2012) 6974–6982.
[31] L. Manna, D.J. Milliron, A.P. Alivisatos, Nat. Mater. 2 (2003) 382–385.
[32] P. Zhou, J.G. Yu, Y.X. Wang, Appl. Catal. B: Environ. 142–143 (2013) 45–53.
[33] T.L. Bahers, M. Reírat, P. Sautet, J. Phys. Chem. C 118 (2014) 5997–6008.
[34] J.W. Tang, J.H. Ye, Chem. Phys. Lett. 410 (2005) 104–107.
[35] P. Zhou, J. Wu, W. Yu, G. Zhao, G. Fang, S. Cao, Appl. Surf. Sci. 319 (2014) 167–172.
[36] L.J. Zhao, X.C. Zhang, C.M. Fan, Z.H. Liang, P.D. Han, Physica B 407 (2012) 3364–3370.
[37] G. Hautier, A. Jain, S.P. Ong, J. Mater. Sci. 47 (2012) 7317–7340.
[38] A. Peles, J. Mater. Sci. 47 (2012) 7542–7548.
[39] L.J. Sham, M. Schlüter, Phys. Rev. Lett. 51 (1983) 1888–1891.
[40] A.J. Cohen, P. Mori-Sánchez, W. Yang, Phys. Rev. B 77 (2008) 115123.
[41] J.G. Yu, P. Zhou, Q. Li, Phys. Chem. Chem. Phys 15 (2013) 12040–12047.
[42] J. Muscat, A. Hung, S. Russo, I. Yarovsky, Phys. Rev. B 65 (2002) 054107.
[43] F.G. Wang, C.D. Valentin, G. Pacchioni, J. Phys. Chem. C 115 (2011) 8345–8353.
[44] M.D. Segall, P.J.D. Lindan, M.J. Probert, C.J. Pickard, P.J. Hasnip, S.J. Clark, M.C. Payne, J. Phys.: Condens. Matter 14 (2002) 2717–2744.
[45] W.l. Huang, J. Comput. Chem. 30 (2009) 1882–1891.
[46] C.-Y. Yeh, Z.W. Lu, S. Froyen, A. Zunger, Phys. Rev. B 46 (1992) 10086.
[47] D. Rodic, V. Spasojevic, A. Bajorek, P. Onnerud, J. Magn. Magn. Mater. 152 (1996) 159–164.
[48] C. Ricolleau, L. Audinet, M. Gandais, T. Gacoin, Eur. Phys. J. D 9 (1999) 565–570.
[49] P. Liao, E.A. Carter, Chem. Soc. Rev. 42 (2013) 2401–2422.
[50] M. Dong, J.F. Zhang, J. Yu, APL Mater. 3 (2015) 104404.
[51] J.P. Perdew, M. Levy, Phys. Rev. Lett. 51 (1983) 1884–1887.
[52] Z.Y. Zhao, W.W. Dai, Inorg. Chem. 53 (2014) 13001–13011.
[53] E.M. Patterson, C.E. Shelden, B.H. Stockton, Appl. Opt. 16 (1977) 729–732.
[54] J.F. Zhang, W.L. Yu, J.J. Liu, B.S. Liu, Appl. Surf. Sci. 358 (2015) 457–462.
[55] W.L. Yu, J.F. Zhang, T.Y. Peng, Appl. Catal. B: Environ. 181 (2016) 220–227.
[56] Z.J. Li, Y. Dai, X.C. Ma, Y.T. Zhu, B.B. Huang, Phys. Chem. Chem. Phys. 16 (2014) 3267–3273.
[57] X.C. Ma, Y. Dai, M. Guo, B.B. Huang, ChemPhysChem 13 (2012) 2304–2309.
[58] J.F. Zhang, P. Zhou, J.J. Liu, J.G. Yu, Phys. Chem. Chem. Phys 16 (2014) 20382–20386.
[59] Z. Yang, D. Gao, Z. Zhu, J. Zhang, Z. Shi, Z. Zhang, D. Xue, Nanoscale Res. Lett. 8 (2013) 17.